The Astrophysical Journal, 633:1191–1200, 2005 November 10

ANNULAR GROOVE PHASE MASK CORONAGRAPH

D. Mawet,[1] P. Riaud,[2] O. Absil,[3] and J. Surdej
Institut d'Astrophysique et de Géophysique, Université de Liège, 17 Allée du 6 Août, Bât B5c, B-4000 Liège, Belgium;
mawet@astro.ulg.ac.be, riaud@astro.ulg.ac.be, absil@astro.ulg.ac.be, surdej@astro.ulg.ac.be
Received 2005 May 10; accepted 2005 July 17

ABSTRACT

We present a new phase mask coronagraph consisting in an optical vortex induced by a space-variant surface relief subwavelength grating. Phase mask coronagraphy is a recent technique aiming at accommodating both high dynamic and high angular resolution imaging of faint sources around bright objects such as exoplanets orbiting their parent stars or host galaxies of active galactic nuclei. Subwavelength gratings are known to be artificially birefringent. Their unique dispersive characteristics can be controlled through the grating geometry in order to synthesize achromatic phase shifters. We show that implementing them in a ring-shaped way produces a fully symmetric and achromatic coronagraph without any gap or "dead zone." The practical manufacturing of the device is also discussed.

Subject headings: circumstellar matter — planetary systems — techniques: high angular resolution

1. INTRODUCTION

Direct detection of faint sources around bright astrophysical objects such as stars or active galactic nuclei (AGN) is very difficult due to the large flux ratio between them. For example, an Earth-like exoplanet is typically 6×10^9 times fainter than its host star in the visible and 7×10^6 times fainter in the thermal infrared, while the contrast of already known debris disks around main-sequence stars is generally larger than 1000 in the visible (e.g., β Pictoris's disk; see Smith & Terrile 1984). The circumnuclear structures of AGNs (obscuring torus, jet-induced structures, etc.) are at least 100 times less luminous than the central engine at visible and near-IR wavelengths (e.g., NGC 1068; see Rouan et al. 2004, for instance). The study of such objects therefore requires dedicated instruments such as coronagraphs. Current coronagraph designs are either pure amplitude masks (Lyot 1939) or pure phase masks (Roddier & Roddier 1997; Rouan et al. 2000; Soummer et al. 2003). Let us mention the special case of the achromatic interferocoronagraph (AIC; Gay & Rabbia 1996), which consists of a single-pupil achromatic nulling interferometer and also the so-called vortex spatial filter, which is a monochromatic pupil plane mask (Swartzlander 2001). The phase mask coronagraphs have been designed as alternative solutions to the amplitude coronagraphs to correct their inherent weakness: the physical extension of the opaque zone occults quite a significant fraction of the central field and thus all sources located behind it, i.e., near the bright object.

The four-quadrant phase mask coronagraph (FQ-PM) proposed by Rouan et al. (2000) is a very well performing design. The principle is to divide the focal plane into four equal areas centered on the optical axis, with two of them on a diagonal providing a π phase shift. This causes destructive interference ("nulling") to occur inside the geometric pupil area. The FQ-PM coronagraph has been validated on a laboratory bench in monochromatic light (Riaud et al. 2003) and installed on the NAOS-CONICA adaptive optics instrument (Boccaletti et al. 2004) at the ESO's Very Large Telescope (VLT). It has given promising preliminary scientific results (Gratadour et al. 2005) and perspectives for future instruments such as the European Mid-IR Instrument for NASA's *James Webb Space Telescope* (Baudoz et al. 2005) or the VLT Planet Finder, a second-generation instrument for the VLT (Mouillet et al. 2003). Unfortunately, the FQ-PM still possesses two drawbacks. First, the π phase shift is difficult to achieve in practice without or with a low chromaticity. Several solutions have nevertheless been studied; a very promising one we have recently proposed uses the unique dispersive characteristics of subwavelength gratings (Mawet et al. 2005). Second, the four phase transitions between adjacent quadrants create four λ/D-large "dead zones," where the potential circumstellar signal or companion is attenuated by up to 4 mag (Riaud et al. 2001).

In this paper, we propose a new design of a phase mask coronagraph derived from the FQ-PM that inherently allows the reduction of the chromaticity issues down to an acceptable level and totally suppresses the annoying dead zones of the latter. This new coronagraph is referred to as the annular groove phase mask (AGPM) coronagraph, since it is made up of a concentric circular subwavelength grating (see Fig. 1). The paper is organized as follows. In § 2 we present the principles of the AGPM coronagraph by introducing the subwavelength gratings, describing their so-called space-variant implementation, and finally discussing the chosen design. Section 3 is devoted to the realistic numerical simulations of the AGPM performance based on a three-stage modeling. In § 4 we briefly provide some manufacturing hints. Finally, we conclude by giving some perspectives on future applications in § 5. Some results and mathematical developments are detailed in the appendices.

2. PRINCIPLES OF THE AGPM CORONAGRAPH

The AGPM coronagraph is a focal plane microcomponent consisting of a concentric circular surface-relief grating with rectangular grooves of depth h equally separated by the period Λ (see Fig. 1). This coronagraph, working in natural light, is a pure vectorial phase mask, i.e., it induces a differential phase shift between the local polarization components of the incident natural (or polarized) light. As for every other coronagraph, the AGPM coronagraph is complemented by a well-dimensioned diaphragm

[1] Ph.D. student, under "FRIA" contract.
[2] Postdoctoral position, under "PAI" contract.
[3] Ph.D. student, under "FNRS" contract.

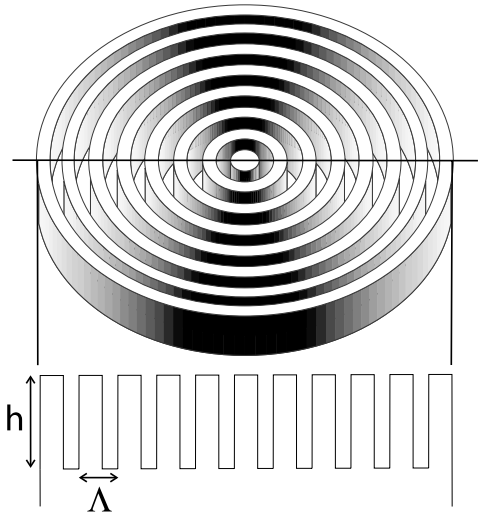

FIG. 1.—AGPM coronagraph scheme. The AGPM consists of a concentric circular surface-relief subwavelength grating with rectangular grooves of depth h and a periodicity Λ.

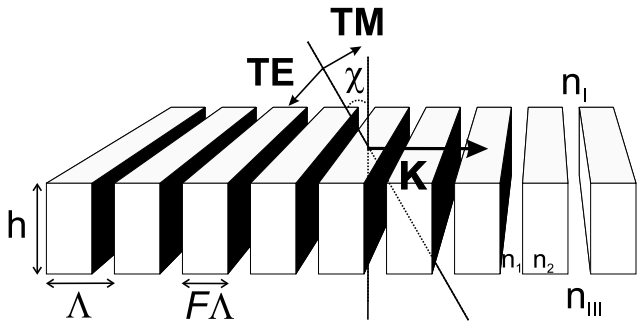

FIG. 3.—ZOG scheme presenting the main grating parameters: the grating vector $|\boldsymbol{K}| = 2\pi/\Lambda$, perpendicular to the grating lines, where Λ is the period; the grating depth h; and the so-called filling factor F, such that $F\Lambda$ is the width of the grating ridges. The vectors **TE** and **TM** are the vectorial orthogonal polarization components of the χ-incident light. Here $n_{\rm I}$ and $n_{\rm III}$ are the refractive indices of the incident and transmitting media, respectively. The parameters n_1 and n_2 are the refractive indices of the grating itself (in our case, $n_1 = n_{\rm I}$ and $n_2 = n_{\rm III}$). Finally, **TE** is the transverse electric vibration, where the electric field vector is perpendicular to the plane of incidence (the plane of incidence is defined by the grating normal and the direction of the incoming light, in our case by the grating normal and the grating vector), and **TM** is the transverse magnetic one (the electric field vector lies in the plane of incidence).

in the relayed pupil plane (Lyot stop) to suppress the diffracted starlight (for the optical implementation, see Fig. 2).

2.1. *Subwavelength Gratings*

When the period Λ of the grating is smaller than the wavelength of the incident light, it does not diffract as a classical spectroscopic grating. All the incident energy is forced to propagate only in the zeroth order, leaving incident wave fronts free from any further aberrations. The subwavelength gratings are therefore often called zeroth-order gratings (ZOGs). Whether a diffraction order propagates or not is determined by the well-known grating equation, from which a "ZOG condition" on the grating period to wavelength ratio can be derived,

$$\frac{\Lambda}{\lambda} \leq \frac{1}{n_{\rm I} \sin\chi + \max(n_{\rm I}, n_{\rm III})}, \tag{1}$$

where χ is the angle of incidence and $n_{\rm I}$ and $n_{\rm III}$ are the refractive indices of the incident (superstrate) and transmitting (substrate) media, respectively (see Fig. 3). This type of grating behaves like homogeneous media with unique characteristics, which can be used to synthesize artificial birefringent achromatic wave plates (Kikuta et al. 1997; Nordin & Deguzman 1999) or monolithic antireflective structures (see, e.g., Karlsson & Nikolajeff 2003). Quarter-wave or half-wave plates are extensively used in astrophysics for polarimetric studies. Subwavelength gratings constitute an elegant and flexible solution to produce these plates.

The key point is that by carefully controlling the geometry of the grating structure (via the grating parameters: the period Λ, the depth h, and the width of the grating ridges $F\Lambda$, where F is the filling factor), one can finely adjust the so-called form birefringence

$$\Delta n_{\rm TE-TM}(\lambda) = n_{\rm TE}(\lambda) - n_{\rm TM}(\lambda), \tag{2}$$

where $n_{\rm TE}$ and $n_{\rm TM}$ are the two effective indices associated with the subwavelength structure, one for each polarization state: **TE** (transverse electric, see Fig. 3) and **TM** (transverse magnetic). Intuitively, one can understand this artificial anisotropy and the existence of two distinct effective indices: the incident light sees two different media as its vectorial components vibrate parallel or orthogonal to the grating lines. The goal is to make the form birefringence proportional to the wavelength in order to compensate for the hyperbolic dependence of the subsequent differential phase shift between the two polarization components **TE** and **TM** and thus achromatize it at the required value of π,

$$\Delta\phi_{\rm TE-TM}(\lambda) = \frac{2\pi}{\lambda} h \Delta n_{\rm TE-TM}(\lambda) \approx \pi, \tag{3}$$

where h is the optical path through the birefringent medium.

2.2. *Space-variant ZOGs*

The concentric circular grooves of the AGPM coronagraph are in fact what is called a "space-variant" ZOG: when the local characteristics (period, orientation of the grating lines, etc.) of the structure vary from point to point, it is said to be space variant. Such components were recently extensively studied as polarization control elements (Niv et al. 2003; Biener et al. 2002;

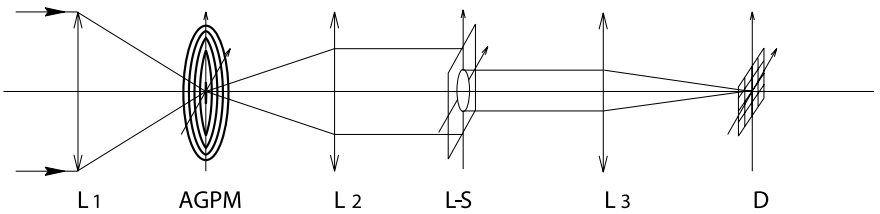

FIG. 2.—Basic AGPM coronagraphic optical bench scheme. L1, L2, and L3 are three lenses in the optical system. L1 provides a large (to minimize spatial defects) F/d ratio on the AGPM, L2 images the pupil in the second plane, the Lyot stop (L-S) suppresses the diffracted starlight, and finally L3 forms the coronagraphic image on the detector D.

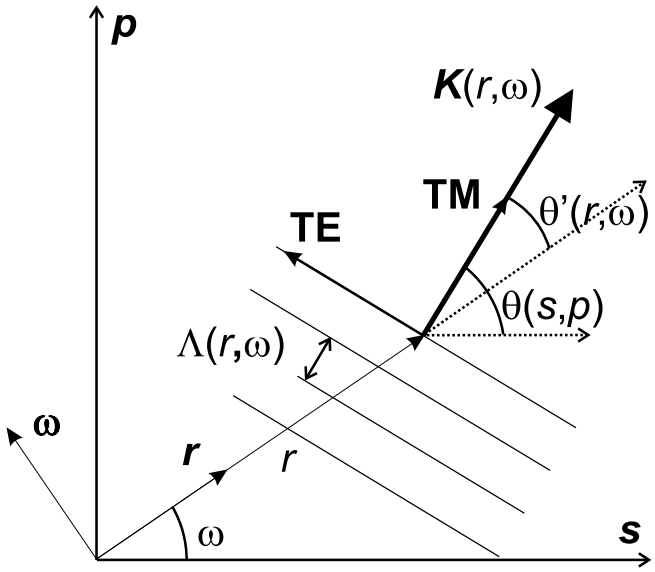

FIG. 4.—Space-variant ZOG vectorial analysis. Here $\boldsymbol{s}$ and $\boldsymbol{p}$ are the unit vectors of the chosen Cartesian basis, whereas $\boldsymbol{\omega}$ and $\boldsymbol{r}$ are the polar coordinate unit vectors. In addition, **TE** (transverse electric) and **TM** (transverse magnetic) are the polarization unit vectors according to the local grating line orientations. By definition, in normal incidence, the **TE** (**TM**) components are orthogonal (parallel) to the local grating vector $\boldsymbol{K}(s,p)$ [$=\boldsymbol{K}(\omega,r)$], spanning angles $\theta(s,p)$ and $\theta'(\omega,r)$ with respect to $\boldsymbol{s}$ and $\boldsymbol{r}$, respectively. Finally, $\Lambda(s,p)$ [$=\Lambda(\omega,r)$] is the grating period.

Bomzon et al. 2002; Levy et al. 2004). Applications are numerous: for example, polarimetry, laser-beam shaping, laser machining, tight focusing, particle acceleration, and atom trapping. Space-variant ZOGs are typically described by a function representing the grating vector spatial variation,

$$\boldsymbol{K}(s,p) = K_0(s,p)[\cos\theta(s,p)\boldsymbol{s} + \sin\theta(s,p)\boldsymbol{p}], \qquad (4)$$

where $\boldsymbol{s}$ and $\boldsymbol{p}$ are the Cartesian unit vectors and $K_0(s,p) = 2\pi/\Lambda(s,p)$ is the grating vector modulus corresponding to the local period $\Lambda(s,p)$. Here $\theta(s,p)$ is the local direction of the grating vector with respect to $\boldsymbol{s}$, the space-variant grating vector always being perpendicular to the local grating lines (see Fig. 4). In polar coordinates, we have

$$\boldsymbol{K}(r,\omega) = K_0(r,\omega)[\cos\theta'(r,\omega)\boldsymbol{r} + \sin\theta'(r,\omega)\boldsymbol{\omega}], \qquad (5)$$

where $\boldsymbol{r}$ and $\boldsymbol{\omega}$ are the polar coordinate unit vectors. Here $\theta'(\omega,r)$ is the local direction of the grating vector with respect to $\boldsymbol{r}$ (see Fig. 4). Let us now consider the general case of the spiral geometric phase space-variant ZOGs. The grating groove direction in this case is given by $\theta(s,p) = l_p\omega/2$ or $\theta'(r,\omega) = (l_p/2-1)\omega$, where l_p is the so-called topological Pancharatnam charge (a nonsigned integer; see Appendix B). The grating vector therefore becomes

$$\boldsymbol{K}(r,\omega) = K_0(r,\omega)\{\cos[(l_p/2-1)\omega]\boldsymbol{r} + \sin[(l_p/2-1)\omega]\boldsymbol{\omega}\}. \qquad (6)$$

The continuity of the grating grooves is ensured by imposing $\nabla \times \boldsymbol{K} = 0$, which also implies that the grating vector derives from a grating function Φ ($\boldsymbol{K} = \nabla\Phi$). Integration over an arbitrary path yields

$$\Phi(r,\omega) = \begin{cases} 2\pi\dfrac{r_0}{\Lambda_0}\left(\dfrac{r_0}{r}\right)^{l_p/2-1}\dfrac{\cos(l_p/2-1)\omega}{(l_p/2-1)}, & l_p \neq 2, \\ 2\pi\dfrac{r_0}{\Lambda_0}f(r), & l_p = 2. \end{cases} \qquad (7)$$

This function describes a family of binary gratings depending on the topological charge l_p (Fig. 5). Let us remark that the continuity criterion has been introduced for manufacturing convenience. In the $l_p = 2$ case, the circular symmetry allows the choice of any pure radial function. The AGPM corresponds to

$$\Phi_{\mathrm{AGPM}}(r,\omega) = 2\pi\frac{r}{\Lambda_0}, \quad l_p = 2. \qquad (8)$$

The family of spiral phase space-variant ZOGs creates an "optical vortex." Indeed, at the center of these components, the phase possesses a screw dislocation inducing a phase singularity, i.e., an optical vortex. The central singularity forces the intensity to vanish by a total destructive interference, creating a dark core. This dark core propagates and is conserved along the optical axis. Whether a dark core is created in the pupil or focal plane of a telescope will determine the way it further evolves. Swartzlander (2001) proposed to create an optical vortex in the pupil plane to peer at the faint monochromatic signal in the relayed focal plane with appropriate filtering. In this paper, we propose to do the inverse, i.e., to create an optical vortex in the focal plane, filter in the relayed pupil plane, and make the detection in a final image plane. This solution is theoretically much more attractive, as we will see. Furthermore, the ZOG's unique properties permit an efficient broadband use.

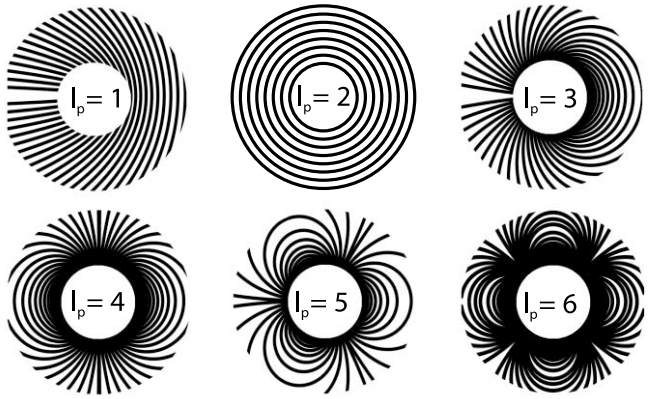

FIG. 5.—Binary grating geometry for topological charges l_p ranging from 1 to 6. Only the $l_p = 2$ geometry possesses the required circular symmetry for use with constant ZOG parameters, which permit achromatization. The component centers have been occulted for presentation purposes.

2.3. *AGPM Coronagraph*

The AGPM coronagraph corresponds to the spiral phase of topological charge $l_p = 2$, implying that the Pancharatnam phase (see Appendix B) undergoes two 2π phase jumps within one revolution around the optical axis (see Fig. 6). This phase modification results solely from the polarization manipulation and is purely geometrical in nature. In the $l_p = 2$ case, a given polarization state repeats itself $2l_p = 4$ times. This point is argued for the linear polarization case in § A1 (a full analytical treatment of the polarization using space-variant Jones matrices is presented in Appendix A). We also show in § A2 that the

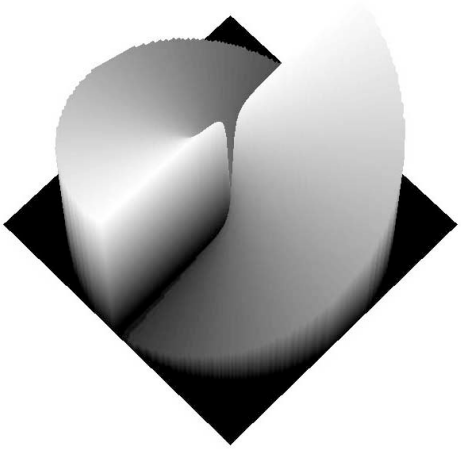

FIG. 6.—Pancharatnam phase ramp of the AGPM coronagraph: $\phi_p = 2\omega$. The associated topological charge is $l_p = 2$. Within one revolution around the optical axis, i.e., $\omega = 2\pi$, one easily confirms that $\phi_p = 2(2\pi)$.

Jones vector for the output components can also be described in a helical polarization basis, with right-handed ($\boldsymbol{R}^{\circlearrowright}$) and left-handed ($\boldsymbol{L}^{\circlearrowleft}$) circularly polarized input fields. In this particular case and under ideal conditions, we obtain at the output

$$\boldsymbol{R}^{\circlearrowright} = \begin{bmatrix} 0 \\ e^{i(2\omega-\pi/2)} \end{bmatrix}, \quad \boldsymbol{L}^{\circlearrowleft} = \begin{bmatrix} e^{-i(2\omega+\pi/2)} \\ 0 \end{bmatrix}. \tag{9}$$

The Pancharatnam phase clearly appears as the argument of the exponential, $\phi_p = 2\omega$. Therefore, within one revolution, i.e., $\omega = 2\pi$, one easily confirms that $\phi_p = 2(2\pi)$. In addition, the helical basis allows us to decouple the output polarization components. This facilitates the forthcoming Fourier analysis.

We demonstrate in Appendix C, thanks to Sonine's integral (Sneddon 1951, p. 55), that in the $l_p = 2$ configuration the vortex propagation up to the relayed pupil plane evolves into a perfect destructive interference, totally rejecting the starlight outside the geometric pupil area (we also analytically demonstrate that the perfect attenuation holds true for even values of l_p). Like the FQ-PM, the theoretical attenuation of the AGPM is therefore infinite in the perfect achromatic and circular filled pupil case (Riaud et al. 2001). We have also chosen the $l_p = 2$ case for the following reason: in order to be achromatic, the space-variant ZOG local characteristics (grating period, depth, and filling factor) are well defined and do not tolerate any departure from optimal values within the tolerances (see § 4). We note in Figure 5 that only the $l_p = 2$ case affords the required symmetry to fulfill this constraint. The other configurations ($l_p \neq 2$) all imply a variation of the grating period that would destroy the achromatic characteristics of the phase shift. Moreover, such a variation of the period could lead the grating to exit the subwavelength domain with dramatic consequences: higher diffraction orders would show up.

The AGPM implementation of the space-variant ZOG is thus totally circularly symmetric. The grating vector is constant in modulus and aligned with the radius. In other words, the AGPM coronagraph can be seen as a FQ-PM coronagraph in polarization. Indeed, if we consider the four cardinal points on the AGPM, the resulting phase shift distribution is analogous to the FQ-PM for each parallel potentially interfering polarization state (see Fig. 7). This argument holds true for each azimuth angle and for each radius, and thus for the whole focal plane.

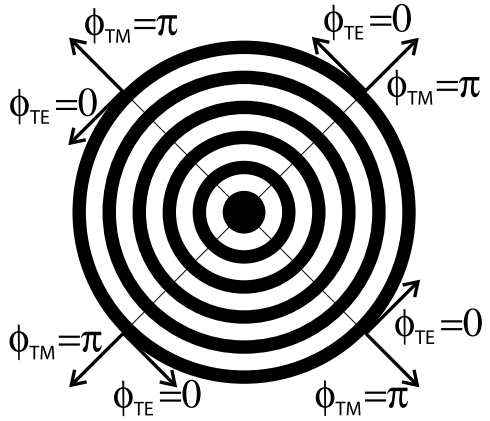

FIG. 7.—AGPM scheme and analogy with the FQ-PM coronagraph. The AGPM can be seen as a polarization FQ-PM. The parallel potentially interfering polarization states are out of phase according to the FQ-PM focal plane phase shift distribution. Here $\phi_{\rm TE}$ and $\phi_{\rm TM}$ are the output phases of the polarization components **TE** and **TM** such that $\Delta\phi_{\rm TE-TM} = |\phi_{\rm TE} - \phi_{\rm TM}| = \pi$.

3. NUMERICAL RESULTS IN A REALISTIC CASE

We have performed realistic numerical simulations that rely on a three-stage modeling:

1. A "rigorous coupled wave analysis" stage, where the form birefringence of the local grating is optimized, leading to the space-variant ZOG Jones matrix $J_{\rm ZOG}(s, p)$. At this stage, the final performance of the coronagraph can already be quantified by the null depth.
2. The analytical polarization treatment based on Jones calculus, which gives the spatial distribution of the linear/helical polarization components of the incident light. We use for this step the results obtained in Appendix A.
3. A scalar far-field Fourier propagation coronagraphic code for each polarization state.

To simulate the grating response and calculate the form birefringence $\Delta n_{\rm form} = \Delta n_{\rm TE-TM}$ in the subwavelength and resonant domain ($\Lambda \approx \lambda$), scalar theories of diffraction dramatically fail. The vectorial nature of light must be taken into account, implying a resolution of the Maxwell equations by the so-called rigorous coupled wave analysis (RCWA; Moharam & Gaylord 1981). RCWA gives the full diffractive characteristics of the simulated structure.

The ZOG form birefringence optimization has already been extensively presented in Mawet et al. (2005) in the context of the FQ-PM achromatization for the *H*, *K*, and *N* bands (4QZOG). We focus here on the mostly used *K* band, but the conclusions are applicable to other band filters. In Figure 8 we present the RCWA results for a subwavelength surface-relief grating engraved on the surface of a diamond (C) or ZnSe substrate and covered by a $\approx\lambda/4$ antireflective (AR) layer of YF_3. The latter settles at the bottom of the grooves and on top of the grating ridges. The null depth, which characterizes the darkness of the destructive interference taking place in the relayed pupil plane of the telescope, takes into account the phase errors with respect to π, $\epsilon(\lambda) = \Delta\phi_{\rm TE-TM}(\lambda) - \pi$, and amplitude mismatches $q(\lambda) = \eta_{\rm TE}(\lambda)/\eta_{\rm TM}(\lambda)$ in the following way:

$$N(\lambda) = \frac{\left[1 - \sqrt{q(\lambda)}\right]^2 + \epsilon(\lambda)^2\sqrt{q(\lambda)}}{\left[1 + \sqrt{q(\lambda)}\right]^2}. \tag{10}$$

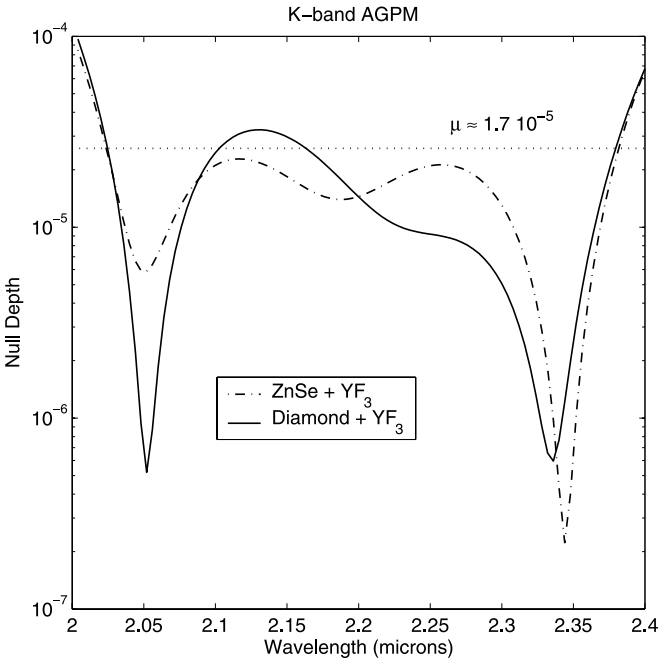

FIG. 8.—*K*-band AGPM coronagraph null depth vs. wavelength. The solid curve is for the diamond YF_3 AR coated ZOG. The dot-dashed curve is for the ZnSe YF_3 AR coated one. The mean null depth over the whole *K* band is $\mu \approx 1.7\times10^{-5}$.

We can notice in Figure 7 the efficiency of the ZOG solution in solving the chromaticity problem for the *K* band with a mean null depth $\mu \approx 1.7\times10^{-5}$. As said before, deep nulls can also be achieved for other usual band filters (see Table 1). It must be noted that the optical throughput efficiency of the optimized ZOG is >90%. For the sake of clarity, the third stage of the AGPM simulations (Fourier propagation) has been performed for the *K* band only. We have used an IDL code for Fraunhofer diffraction analysis (Riaud et al. 2001). To minimize the aliasing effect of the fast Fourier transform, we have used large arrays (up to 2048×2048) for the calculation. The intrinsic performance of the coronagraph will be limited by the phase residuals with respect to π and the transmittance mismatches between the two polarization states **TE** and **TM**, as well. We have also assumed wave front qualities of $\lambda_0/250$ rms, where λ_0 is the central wavelength of the considered filter. In our case (*K* band: $\lambda_0 = 2.2$ μm), this hypothesis leads therefore to wave front qualities of $\approx\lambda/70$ rms, with $\lambda = 632.8$ nm. This is quite a severe but somewhat realistic figure. Indeed, the Virgo team (Mackowski et al. 1999; Brillet et al. 2003) has demonstrated state-of-the-art mirror quality with an excellent polishing realization ($\lambda/226$ rms at 632.8 nm) within the framework of gravitational wave detection. This technology is directly applicable to our case.

The final results of our three-stage calculation are excellent (see Fig. 9). As demonstrated in Appendix C in an analytical way, the starlight is rejected outside the geometric pupil area in a fully symmetric annular shape. The smoothness of the phase shift occurring in the focal plane ensures the absence of the dead zones induced by the FQ-PM/4QZOG quadrant transitions. The final *K*-band polychromatic image reveals the simulated companion 15 mag fainter. The coronagraphic profile functions of the angular separation in λ/d (d is the telescope diameter) show a peak-to-peak attenuation of about 10^{-5} (Fig. 10). The speckle level of $\approx10^{-7}$ is quickly reached at a few λ/d. The AGPM coronagraphic behavior is very similar to the achromatic 4QZOG coronagraph (Mawet et al. 2005), but with a total symmetry.

Figure 11 presents the attenuation of the off-axis simulated companion, which is also quite similar to the FQ-PM/4QZOG in its best configuration, i.e., only along the two diagonals. Indeed, as mentioned in the introduction, the FQ-PM/4QZOG quadrant transitions induce a nonnegligible attenuation of the superimposed circumstellar features lying on them. These dead zones represent quite a significant portion of the focal plane (about 10% at $6\lambda/d$). Thanks to the perfect AGPM circular symmetry, this problem does not exist anymore. We also note that the inner working angle of the AGPM is very good, peering well under λ/d. As far as stellar leakage is concerned, numerical simulations show that it increases as $\theta^2_{\lambda/d}$ close to the optical axis, just as the FQ-PM/4QZOG (where $\theta_{\lambda/d}$ is the angle from the optical axis). In fact, calculations show that for a vortex of topological charge l_p, the stellar leakage grows as $\theta^{l_p}_{\lambda/d}$.

4. MANUFACTURING

In the *K*-band diamond AGPM case, for instance, the local ZOG optimal parameters are

1. period, $\Lambda = 740$ nm;
2. filling factor, $F = 70\%$;
3. total depth, $h = 3.240$ μm; and
4. AR layer thickness, 420 nm.

The fabrication of the AGPM coronagraph implies no developments other than those for the 4QZOG (Mawet et al. 2005), which is currently under assessment in diamond by Uppsala University's Angström Laboratory "Adamantis AB" (Karlsson

TABLE 1
AGPM ACHROMATIZATION (NULL DEPTH) FOR VARIOUS BAND FILTERS: VISIBLE, NEAR-IR AND MID-IR

PARAMETER	FILTER			
	V ($R_\lambda = 5.5$)	*I* ($R_\lambda = 3.75$)	*J* ($R_\lambda = 4.16$)	*H* ($R_\lambda = 4.7$)
Null depth (on-axis)	2×10^{-5}	1.35×10^{-4}	6.5×10^{-5}	3.5×10^{-5}
Expected contrast (at $3\lambda/d$)	1.66×10^{-7}	1.12×10^{-6}	5.42×10^{-7}	2.92×10^{-7}
Grating period (nm)	280 (n-LAF32)	305 (C)	400 (C)	525 (C)
	K ($R_\lambda = 5.5$)	*L'* ($R_\lambda = 6.3$)	*M* ($R_\lambda = 16.6$)	*N* ($R_\lambda = 4.86$)
Null depth (on-axis)	1.7×10^{-5}	8.4×10^{-6}	5×10^{-7}	4×10^{-5}
Expected contrast (at $3\lambda/d$)	1.42×10^{-7}	7×10^{-8}	4.2×10^{-9}	3.3×10^{-7}
Grating period (μm)	0.740 (C)	1.28 (C)	1.7194 (C)	3.29 (C)

NOTES.—Here $R_\lambda = \lambda/\Delta\lambda$ is the spectral resolution. C stands for CVD diamond, while n-LAF32 refers to a high-index Schott glass.

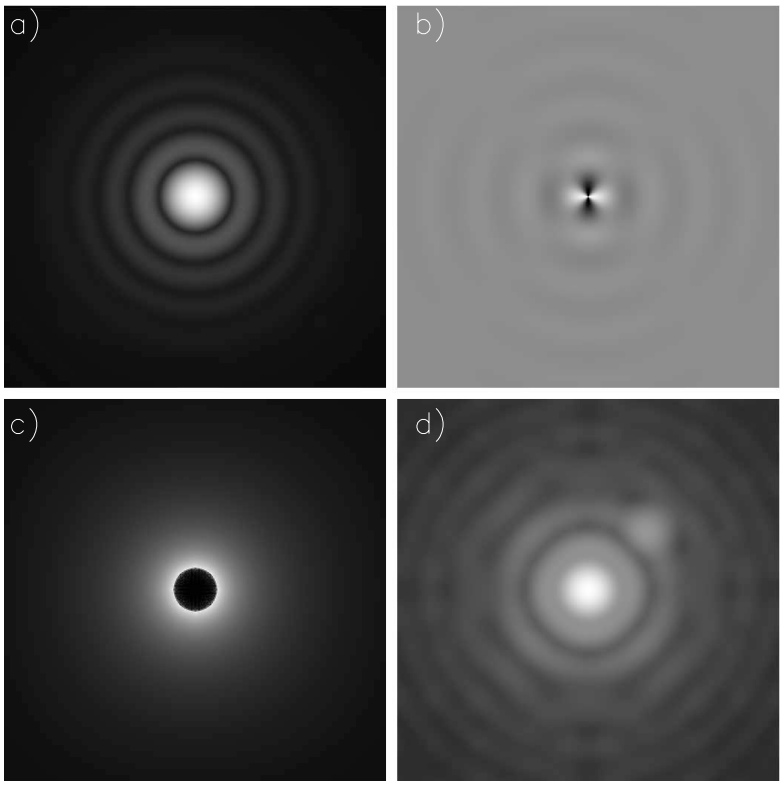

FIG. 9.—Numerical simulation illustrating the diffractive behavior of the AGPM coronagraph. (*a*) Airy pattern provided by a perfect telescope without central obscuration. We have also added a companion 15 mag fainter located $2\lambda/d$ ($\lambda = 2.2$ μm) away from the star. (*b*) Complex amplitude of the star phase shifted by the mask. We note that the phase mask effect is close to that obtained for the FQ-PM coronagraph, but without any discontinuity left. (*c*) Picture showing the starlight rejection in the relayed pupil plane. The diffraction pattern is annular and symmetric in this configuration. (*d*) Resulting coronagraphic image for the full *K* band, where the fainter companion is clearly visible. All images are displayed with a nonlinear scale.

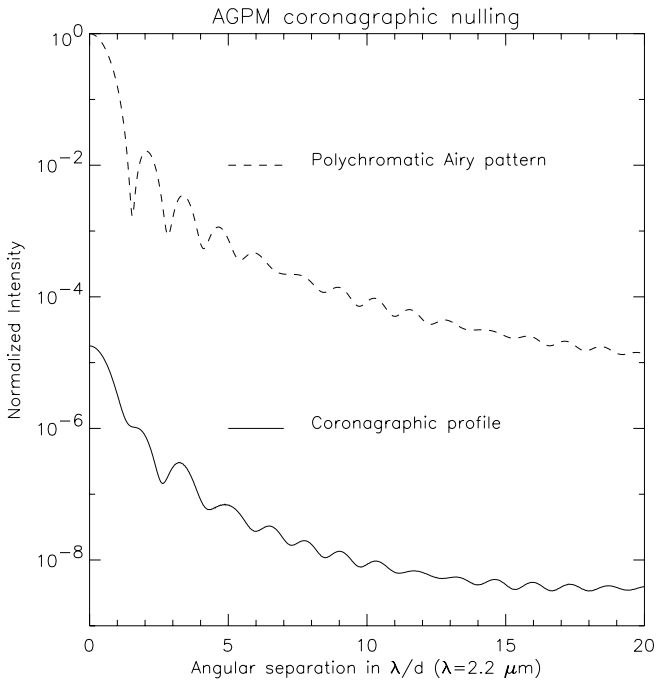

FIG. 10.—Theoretical radial profiles obtained with the *K*-band AGPM. The solid line shows the coronagraphic profile. The residual central peak is due to the effect of the phase errors (residual chromatism) around the π phase shift. In this case, a starlight speckle level of 10^{-7} is reached at $3\lambda/d$. The dashed line shows the polychromatic Airy pattern for the full *K* band. The diaphragm (Lyot stop) is open at 80%.

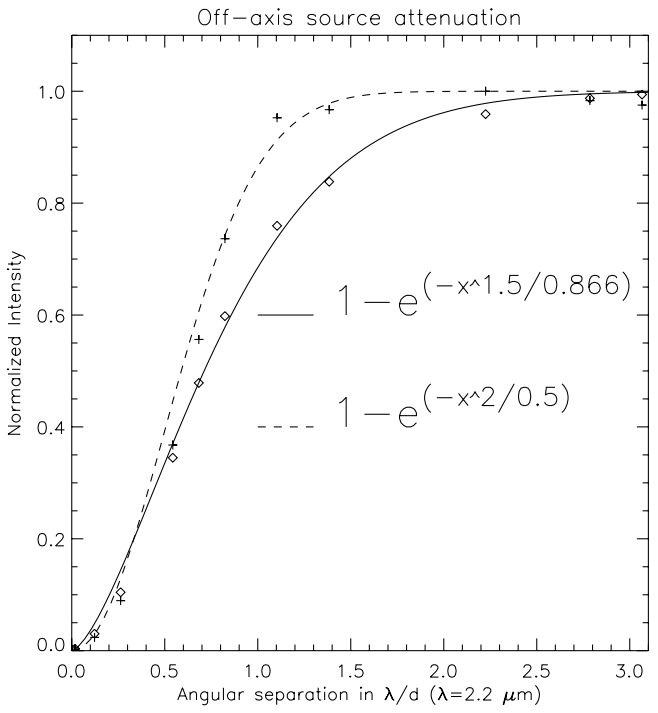

FIG. 11.—Degradation of the coronagraphic performance function of angular separation. This figure compares the companion attenuation for the AGPM vs. the classical 4QZOG in its best configuration, i.e., at least $1\lambda/d$ away from a quadrant transition. This degradation is measured on the total energy. The solid line shows the exponential fit on the simulated data (*open diamonds*) for the AGPM coronagraph. The dashed line shows the exponential fit on the simulated data (*plus signs*) for the FQ-PM/4QZOG coronagraph.

& Nikolajeff 2003; Karlsson et al. 2001). The manufacturing is based on microelectronic technologies. The first step consists in the definition of the lithographic mask: one has to imprint the concentric annular pattern in a resin coated on the chosen substrate material. It can be realized by laser direct writing or *e*-beam lithography. The precision of this step is critical, because it defines once and for all the lateral dimensions of the ZOG, i.e., the filling factor (F). The latter is the determinant parameter of the grating structure and the most difficult to control during the fabrication process. A complete study of the design sensitivity to the parameters has been presented in Mawet et al. (2005). The conclusion was that the tolerance on the filling factor was at the 1% level but also that if the manufacturing process was interactively conducted, then errors on the filling factor definition could be compensated a posteriori. The next fabrication steps consist in transferring the mask pattern into the substrate by an appropriate reactive plasma beam etching down to the desired depth, followed by the $\lambda/4$ AR layer deposition. Assuming a classical realistic resolution of 10 nm in thickness (2%) for the AR layer sputtering, we can ensure a grating etching depth tolerance of about 20 nm at the null depth level of 10^{-5}. This value is well within reach with current technologies, especially if in situ real-time monitoring of the grating parameters is implemented during the fabrication process (Lalanne et al. 1999).

5. DISCUSSION

In this paper, we have presented a new phase mask coronagraph that is free from any "dead zone," thanks to its perfect circular symmetry, and inherently quasi-achromatic. The AGPM coronagraph consists in an optical vortex induced by a space-variant subwavelength grating. The potential performance of the AGPM coronagraph is very good, ensuring, for instance, a theoretical contrast of 1.4×10^{-7} at $3\lambda/d$ over the whole K band with inherent perfect symmetry. The inner working angle of the mask is $\approx\lambda/d$, still with a good contrast of $\approx10^{-5}$. Thanks to the ZOG design flexibility, the AGPM coronagraph can accommodate a large variety of materials and wavelength bands (see Table 1), thus making it an attractive solution for future ambitious high-resolution/high-contrast space- or ground-based imaging facilities. For instance, the AGPM coronagraph could be used alone on a single-pupil telescope either in space or on the ground (with an adaptive optics system) to dramatically enhance the dynamics. It could also be used at the Fizeau or densified focus of an interferometer (Labeyrie 1996; Boccaletti et al. 2000; Riaud et al. 2002) to take advantage of the increased resolution. However, in the Fizeau configuration, phase coronagraphs are limited by the cross-talk between the different interferometer subpupils, whereas in the densified one, the limitation comes from diffraction effects induced by residual gaps between the joined subpupils (P. Riaud et al., in preparation). Nevertheless, the AGPM should be seriously regarded as an integrated high-contrast solution to be implemented in NASA's *Terrestrial Planet Finder* and/or ESA's infrared space interferometer, *DARWIN*, missions.

D. M. acknowledges the financial support of the Belgian "Fonds pour la formation à la Recherche dans l'Industrie et dans l'Agriculture." P. R. and J. S. acknowledge the financial support of the "Pôle d'Attraction Inter-Universitaire."

APPENDIX A

POLARIZATION TREATMENTS

Let us perform a full space-variant polarization and phase analysis of the component, assuming first that it induces an optical vortex of l_pth order. Representing it by a space-variant Jones matrix, one can find the resulting wave front for any incident polarization,

$$J_{\text{vortex}}(s,p) = M[\theta(s,p)]J_{\text{ZOG}}(s,p)M[\theta(s,p)]^{-1}. \tag{A1}$$

Here $J_{\text{ZOG}}(s, p)$ actually describes the effects of the local ZOG form birefringence that transforms the phase (**TE** − **TM** vectorial phase shift $\Delta\phi_{\text{TE-TM}}$) and amplitude (**TE** − **TM** differential Fresnel parasitic reflection) of the outgoing beam,

$$J_{\text{ZOG}}(s,p) = \begin{bmatrix} \eta_{\text{TE}} & 0 \\ 0 & \eta_{\text{TM}}e^{i\Delta\phi_{\text{TE-TM}}} \end{bmatrix}, \tag{A2}$$

where η_{TE} and η_{TM} are the local grating transmittances along the **TE** and **TM** directions of polarization, respectively (the transmittances can be assimilated to diffraction efficiencies). These transmittances are different because of the different Fresnel reflection coefficients resulting from the existence of the two effective indices that give birth to the form birefringence (see eq. [2]). For the sake of simplicity, we write $\Delta\phi = \Delta\phi_{\text{TE-TM}}$. The parameter $M[\theta(s, p)]$ is the θ-dependent rotation matrix

$$M[\theta(s,p)] = \begin{bmatrix} \cos\theta & -\sin\theta \\ \sin\theta & \cos\theta \end{bmatrix}, \tag{A3}$$

where $\theta(s, p)$ is the grating vector angle that defines the local grating line orientations. Thus, we have

$$J_{\text{vortex}}(s,p) = \begin{bmatrix} \eta_{\text{TE}}\cos^2\theta + \eta_{\text{TM}}\sin^2\theta e^{i\Delta\phi} & \sin\theta\cos\theta\left(\eta_{\text{TE}} - \eta_{\text{TM}}e^{i\Delta\phi}\right) \\ \sin\theta\cos\theta\left(\eta_{\text{TE}} - \eta_{\text{TM}}e^{i\Delta\phi}\right) & \eta_{\text{TM}}\sin^2\theta + \eta_{\text{TE}}\cos^2\theta e^{i\Delta\phi} \end{bmatrix}. \tag{A4}$$

In order to carry out the analysis of the component with the scalar Fourier coronagraphic propagation code, we have to chose a basis to project the incident polarization (natural or not).

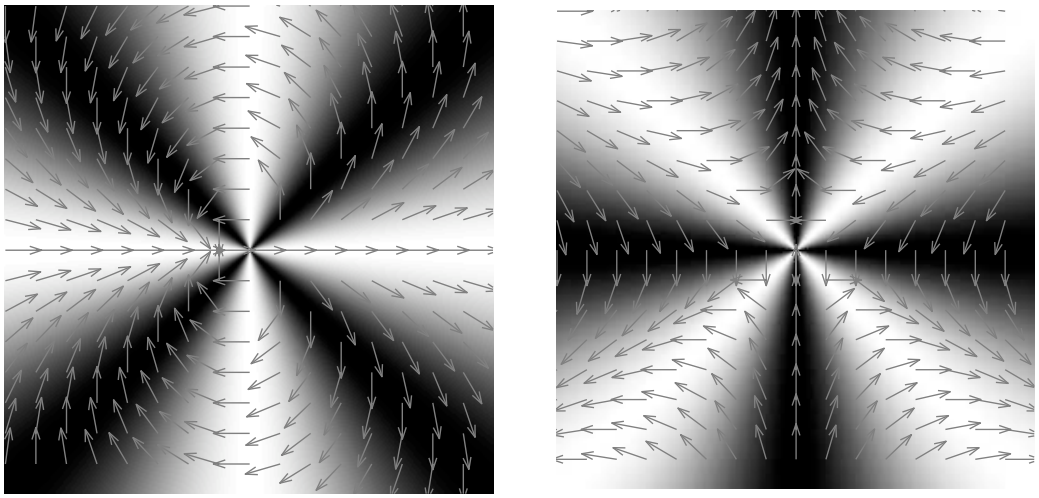

FIG. 12.—AGPM response to linear polarization. *Left:* Intensity map for an input linear horizontal polarization seen by a horizontal analyzer. *Right:* Same, but for an input linear vertical polarization. Arrows show the corresponding vectorial polarization field that has been submitted to the rotation given by eqs. (A9) and (A10). We clearly notice that a given polarization state repeats itself four times.

A1. LINEAR BASIS

We can decompose the problem by projecting the incident polarization on the orthogonal linear ($\boldsymbol{s}, \boldsymbol{p}$) basis. Therefore, we have the following Jones vectors as linear polarization inputs:

$$\boldsymbol{E}_p = \begin{bmatrix} 1 \\ 0 \end{bmatrix}, \tag{A5}$$

$$\boldsymbol{E}_s = \begin{bmatrix} 0 \\ 1 \end{bmatrix}. \tag{A6}$$

Multiplying them both by the vortex Jones matrix $J_{\rm vortex}(s, p)$, we obtain

$$\boldsymbol{E}_p = \begin{bmatrix} \eta_{\rm TE}\cos^2\theta + \eta_{\rm TM}\sin^2\theta e^{i\Delta\phi} \\ \sin\theta\cos\theta\left(\eta_{\rm TE} - \eta_{\rm TM}e^{i\Delta\phi}\right) \end{bmatrix}, \tag{A7}$$

$$\boldsymbol{E}_s = \begin{bmatrix} \sin\theta\cos\theta\left(\eta_{\rm TE} - \eta_{\rm TM}e^{i\Delta\phi}\right) \\ \eta_{\rm TM}\sin^2\theta + \eta_{\rm TE}\cos^2\theta e^{i\Delta\phi} \end{bmatrix}, \tag{A8}$$

respectively, corresponding to the output polarization states to be injected in a subsequent coronagraphic code. In the perfect case (exact π phase shift, i.e., $\Delta\phi_{\rm TE-TM} = \pi$ and unitary matched efficiencies $\eta_{\rm TE} = \eta_{\rm TM} = 1$) for the AGPM configuration ($l_p = 2$ and thus $\theta = l_p\omega/2 = \omega$, where ω is the azimuthal polar coordinate), we have

$$\boldsymbol{E}_p = \begin{bmatrix} \cos 2\omega \\ \sin 2\omega \end{bmatrix}, \tag{A9}$$

$$\boldsymbol{E}_s = \begin{bmatrix} \sin 2\omega \\ -\cos 2\omega \end{bmatrix}. \tag{A10}$$

This implies that in the AGPM case ($l_p = 2$) an input linear polarization, which is horizontal, for example, will locally rotate by twice the azimuthal angle ω, as shown in Figure 12, where the corresponding output vectorial field and intensity response to linear polarization are displayed.

A2. HELICAL BASIS

The analysis can be decoupled by projecting the incident vectorial field on a helical basis, i.e., with right- and left-handed circular polarization unit vectors

$$\boldsymbol{R}^{\circlearrowright} = \begin{bmatrix} 1 \\ 0 \end{bmatrix}, \tag{A11}$$

$$\boldsymbol{L}^{\circlearrowleft} = \begin{bmatrix} 0 \\ 1 \end{bmatrix}. \tag{A12}$$

In such a case, the vortex component Jones matrix must be transformed by

$$J^{\circlearrowleft\circlearrowleft}_{\text{vortex}}(s,p) = UJ_{\text{vortex}}(s,p)U^{-1}, \tag{A13}$$

with the helical-basis transformation matrix

$$U = \frac{1}{\sqrt{2}} \begin{bmatrix} 1 & i \\ 1 & -i \end{bmatrix}. \tag{A14}$$

Finally, we have

$$J^{\circlearrowleft\circlearrowleft}_{\text{vortex}}(s,p) = \frac{1}{2}\left(\eta_{\text{TE}} + \eta_{\text{TM}} e^{i\Delta\phi}\right) \begin{bmatrix} 1 & 0 \\ 0 & 1 \end{bmatrix} + \frac{1}{2}\left(\eta_{\text{TE}} - \eta_{\text{TM}} e^{i\Delta\phi}\right) \begin{bmatrix} 0 & e^{i2\theta} \\ e^{-i2\theta} & 1 \end{bmatrix}. \tag{A15}$$

In the perfect case where $\eta_{\text{TE}} = \eta_{\text{TM}} = 1$ and $\Delta\phi = \pi$, and in the AGPM configuration case where $l_p = 2$ and thus $\theta = l_p\omega/2 = \omega$, where ω is the azimuthal polar coordinate, we obtain as output

$$\boldsymbol{R}^{\circlearrowleft} = \begin{bmatrix} 0 \\ e^{i(2\omega - \pi/2)} \end{bmatrix}, \tag{A16}$$

$$\boldsymbol{L}^{\circlearrowleft} = \begin{bmatrix} e^{-i(2\omega + \pi/2)} \\ 0 \end{bmatrix}. \tag{A17}$$

Therefore, the two output polarization beams are orthogonal and decoupled in the helical basis.

APPENDIX B

PANCHARATNAM TOPOLOGICAL CHARGE

The so-called Pancharatnam phase has been introduced to measure the comparison of the phases of two light beams in different states of polarization. It is defined as the argument of the inner product of the two Jones vectors describing the two light beams to be phase compared,

$$\phi_p = \arg\langle E(\omega, r), E(0, r)\rangle. \tag{B1}$$

We can also define the associated topological charge of the beam, which is a nonsigned integer giving the number of times that the azimuthal angle rotates about the phase disclination (topological defect),

$$l_p = \frac{1}{2\pi} \oint \nabla\phi_p \, ds. \tag{B2}$$

In the AGPM case, $\phi_p = 2\omega$ ($l_p = 2$), which implies that the polarization state repeats itself $2l_p = 4$ times (see Fig. 12).

APPENDIX C

PERFECT REJECTION PROOF

Let us now analytically compute the pupil plane intensity distribution. The latter can be expressed as the Fourier transform of the product of the Airy disk function (a filled circular pupil is assumed) and the mask phase ramp. We have seen in § A2 that the mask phase in the helical basis takes the simple decoupled form $e^{i(l_p\omega - \pi/2)}$. Therefore, in the Fourier-plane polar coordinates (ρ, ψ) we have

$$A_{\text{pup}}(\rho, \psi, l_p) = \text{FT}\left[\frac{2J_1(2\pi R_{\text{tel}} r)}{2\pi R_{\text{tel}} r} e^{i(l_p\omega - \pi/2)}\right](\rho, \psi). \tag{C1}$$

Explicitly,

$$A_{\text{pup}}(\rho, \psi, l_p) = -i \int_0^\infty \int_0^{2\pi} \frac{2J_1(2\pi R_{\text{tel}} r)}{2\pi R_{\text{tel}} r} e^{i(l_p\omega)} e^{-2i\rho r \cos(\omega - \psi)} r \, dr \, d\omega, \tag{C2}$$

where we recognize the nth order Bessel function J_n. Indeed, various integrals can be expressed in terms of Bessel functions,

$$J_n(z) = \frac{1}{2\pi i^{-n}} \int_0^{2\pi} e^{iz\cos\phi} e^{in\phi}\, d\phi, \tag{C3}$$

and thus we have

$$A_{\rm pup}(\rho,\psi,l_p) = -i^{l_p-1}\frac{2e^{il_p\psi}}{R_{\rm tel}} \int_0^{\infty} J_1(2\pi R_{\rm tel} r) J_{l_p}(2\pi\rho r)\, dr. \tag{C4}$$

C1. AGPM CORONAGRAPH: $l_p = 2$

The previous result in the $l_p = 2$ case is the so-called Sonine's integral (Sneddon 1951, p. 55),

$$S = \int_0^{\infty} y^{1+\mu-\lambda} J_\lambda(ay) J_\mu(by)\, dy = \begin{cases} 0, & 0 < a < b, \\ \dfrac{b^\mu (a^2-b^2)^{\lambda-\mu-1}}{2^{\lambda-\mu-1} a^\lambda \Gamma(\lambda-\mu)}, & 0 < b < a. \end{cases} \tag{C5}$$

Thus, taking $l_p = 2$, we have

$$A_{\rm pup}(\rho,\psi,l_p=2) = \begin{cases} 0, & 0 < \rho < R_{\rm tel}, \\ \dfrac{e^{i2\psi}}{\pi\rho^2}, & 0 < R_{\rm tel} < \rho. \end{cases} \tag{C6}$$

We have demonstrated that in the perfect case for $l_p = 2$ (AGPM), the light is entirely rejected outside the geometric pupil area.

C2. GENERALIZATION TO l_pTH-ORDER VORTICES

Equation (C4) corresponds to the so-called Hankel transform of l_pth order of the Bessel J_1 function. This transform has an analytical solution (Abramowitz & Stegun 1972, p. 487),

$$A_{\rm pup}(\rho,\psi,l_p) = -i^{1-l_p}\frac{2e^{il_p\psi}}{R_{\rm tel}} \begin{cases} (2\pi\rho)^{l_p}(2\pi R_{\rm tel})^{-l_p-1} \dfrac{\Gamma(1+l_p/2)}{\Gamma(l_p+1)\Gamma(1-l_p/2)}\, {}_2F_1\left(\dfrac{l_p+1}{2}, \dfrac{l_p}{2}; l_p+1; \dfrac{\rho^2}{R_{\rm tel}^2}\right), & 0 < \rho < R_{\rm tel}, \\ (2\pi\rho)^{-2}(2\pi R_{\rm tel}) \dfrac{\Gamma(1+l_p/2)}{\Gamma(2)\Gamma(l_p/2)}\, {}_2F_1\left(\dfrac{l_p+1}{2}, \dfrac{2-l_p}{2}; 2; \dfrac{\rho^2}{R_{\rm tel}^2}\right), & \rho > R_{\rm tel}, \end{cases} \tag{C7}$$

where we recognize the gamma Γ and hypergeometric ${}_2F_1$ functions. This function shows perfect attenuation for even l_p values only,

$$A_{\rm pup}(\rho,\psi,l_p) = 0, \qquad \rho < R_{\rm tel} \text{ and } l_p = 2, 4, 6, \ldots. \tag{C8}$$

REFERENCES

Abramowitz, M., & Stegun, I. A. 1972, Handbook of Mathematical Functions (New York: Dover)
Baudoz, P., Boccaletti, A., Riaud, P., Cavarroc, C., Baudrand, J., Reess, J. M., & Rouan, D. 2005, PASP, submitted
Biener, G., Niv, A., Kleiner, V., & Hasman, E. 2002, Opt. Lett., 27, 1875
Boccaletti, A., Riaud, P., Baudoz, P., Baudrand, J., Rouan, D., Gratadour, D., Lacombe, F., & Lagrange, A.-M. 2004, PASP, 116, 1061
Boccaletti, A., Riand, P., Moutou, C., & Labeyrie, A. 2000, Icarus, 145, 628
Bomzon, Z., Niv, A., Biener, G., Kleiner, V., & Hasman, E. 2002, Appl. Opt., 41, 5218
Brillet, A., Vinet, J.-Y., Loriette, V., Mackowski, J.-M., Pinard, L., & Remillieux, A. 2003, Phys. Rev. D, 67, 102006
Gay, J., & Rabbia, Y. 1996, CR Acad. Sci. Paris, 332, 265
Gratadour, D., Rouan, D., Boccaletti, A., Riaud, P., & Clénet, Y. 2005, A&A, 429, 433
Karlsson, M., Hjort, K., & Nikolajeff, F. 2001, Opt. Lett., 26, 1752
Karlsson, M., & Nikolajeff, F. 2003, Opt. Express, 11, 502
Kikuta, H., Ohira, Y., & Iwata, K. 1997, Appl. Opt., 36, 1566
Labeyrie, A. 1996, A&AS, 118, 517
Lalanne, P., Pichon, P., Chavel, P., Cambril, E., & Launois, H. 1999, Appl. Opt., 38, 4980
Levy, U., Tsai, C.-H., Pang, L., & Fainman, Y. 2004, Opt. Lett., 29, 1718
Lyot, B. 1939, MNRAS, 99, 580
Mackowski, J. M., Pinard, L., Dognin, L., Ganau, P., Lagrange, B., Michel, C., & Morgue M. 1999, Opt. Quantum Electron., 31, 507
Mawet, D., et al. 2005, Appl. Opt., in press
Moharam, M. G., & Gaylord, T. K. 1981, J. Opt. Soc. Am., 71, 811
Mouillet, D., Fusco, T., Lagrange, A.-M., & Beuzit, J.-L. 2003, in Astronomy with High Contrast Imaging, ed. C. Aime & R. Soummer (Les Ulis: EDP Sciences), 193
Niv, A., Biener, G., Kleiner, V., & Hasman, E. 2003, Opt. Lett., 28, 510
Nordin, G. P., & Deguzman, P. C. 1999, Opt. Express, 5, 163
Riaud, P., Boccaletti, A., Baudrand, J., & Rouan, D. 2003, PASP, 115, 712
Riaud, P., Boccaletti, A., Rouan, D., Lemarquis, F., & Labeyrie, A. 2001, PASP, 113, 1145
Riaud, P., et al. 2002, A&A, 396, 345
Roddier, F., & Roddier, C. 1997, PASP, 109, 815
Rouan, D., Riaud, P., Boccaletti, A., Clénet, Y., & Labeyrie, A. 2000, PASP, 112, 1479
Rouan, D., et al. 2004, A&A, 417, L1
Smith, B. A., & Terrile, R. 1984, Science, 226, 1421
Sneddon, I. N. 1951, Fourier Transforms (New York: McGraw-Hill)
Soummer, R., Dohlen, K., & Aime, C. 2003, A&A, 403, 369
Swartzlander, G. A., Jr. 2001, Opt. Lett., 26, 497